Acta Crystallographica Section A
Foundations of Crystallography
ISSN 0108-7673

Received 11 January 2001
Accepted 20 August 2001

Orbital ordering in $LaMnO_3$: estimates of structure factors and comparison of measurement methods

B. Jiang,[a]* J. M. Zuo,[b] Q. Chen[c] and J. C. H Spence[a]

[a]Department of Physics and Astronomy, Arizona State University, Tempe, AZ 85287, USA, [b]Department of Material Science and Engineering, University of Illinois, Urbana, IL 61801, USA, and [c]Department of Electronics, Beijing University, Beijing 100871, People's Republic of China. Correspondence e-mail: jiangb@asu.edu

This paper shows that the phenomenon of orbital ordering should be detectable by energy-filtered quantitative convergent-beam electron diffraction (QCBED). The structure factors of $LaMnO_3$ crystals are calculated using a non-spherical atomic scattering model of the Mn^{3+} ion. Several low-order electron structure factors showed pronounced change with orbital ordering, in which the e_g^1 electron orders in the $3d(3z^2 - r^2)$ orbital leaving the $3d(x^2 - y^2)$ unoccupied. In contrast, the X-ray structure factors showed very small change. Orbital order is important in transition-metal oxides, including colossal magnetoresistive manganite oxides. The calculations show that by using QCBED it is possible to measure the subtle changes in electron structure factors due to orbital ordering of the e_g^1 electron of the Mn^{3+} ion in an $LaMnO_3$ crystal. A comparison of methods for structure-factor measurement is given, including Bragg X-ray and γ-ray diffraction, X-ray *Pendellösung* and critical-voltage methods. New measurements by QCBED of structure factors in rutile are compared with the Bragg X-ray values. These show that QCEBD can provide an accurate extinction-free measurement of low-order structure factors, which is extremely difficult or perhaps impossible when using other methods applied to real crystals.

1. Introduction

Mn oxides of perovskite-related structure have attracted considerable interest owing to the colossal magnetoresistence effect. Doping the family of compounds $La_{1-x}Ca_xMnO_3$ with divalent Ca^{2+} ions oxidizes Mn^{3+} to Mn^{4+}, introducing holes in the 3*d* valence band that give rise to a series of interesting physical properties, such as charge, orbital and spin ordering, and ferroparamagnetic and metal insulator phase transitions (Goodenough, 1997; Radaelli *et al.*, 1997).

The parent compound $LaMnO_3$ crystal (space group *Pbnm*), with a unit cell of a = 5.5367, b = 5.7473 and c = 7.6929 Å (Rodriguez-Carvajal *et al.*, 1998), is an antiferromagnetic insulator in which orbital ordering is established owing to the cooperative Jahn–Teller (JT) effect breaking the degeneracy of the electronic configuration of Mn^{3+} ($t_{2g}^3 e_g^1$). This particular *C*-type orbital ordering is responsible for the *A*-type magnetic structure observed by Wollan & Koehler (1955). Theoretical simulation has shown that the *A*-type antiferromagnetic state and *C*-type orbital structure (with the pattern of $3x^2 - r^2$ and $3y^2 - r^2$ in $3de_g^1$ orbitals) were stable in a model based on JT phonons, using coupling values physically reasonable for $LaMnO_3$ and considering the small but important effect of octahedral tilting (Hotta *et al.*, 1999). LSDA+U band-structure calculation predicts the same orbital ordering structure (Bala & Oles, 2000). It also showed that the ground state would be a ferromagnetic metal without orbital order, which is contradictory to experiment.

One method of observing orbital ordering is the direct measurement of charge density in crystals. This method requires highly accurate X-ray structure factors. To detect the relatively weak bonding electrons, which mainly contribute at low scattering angles, the accuracy of low-order structure-factor measurement becomes crucial. Recent progress in quantitative energy-filtered convergent-beam electron diffraction (CBED) has made the extinction-free measurement of low-order structure factors possible (Zuo, 1998). Using this method, combined with X-ray diffraction to measure the high-order structure factors, Zuo *et al.* (1999) have directly observed the *d*-orbital holes and Cu—Cu bonding in Cu_2O crystals. The precision of quantitative CBED may also be used to observe the Mn^{3+} ion $3d(3z^2 - r^2)$ orbital ordering.

In this paper, the electron structure factors were calculated using a non-spherical Mn^{3+} ion model with orbital ordering. The effect of $3d(3z^2 - r^2)$ ordering on structure-factor changes was evaluated. This provides a general idea of which diffraction spot is most sensitive to orbital ordering, and therefore needs to be measured by quantitative CBED.

2. Comparison of methods for low-order structure-factor measurement

Several methods have been employed for low-order structure-factor measurement, including (i) the X-ray single-crystal *Pendellösung* method; (ii) conventional Bragg X-ray diffraction; (iii) Bragg γ-ray diffraction at high energies; (iv) quantitative energy-filtered convergent-beam electron diffraction (QCBED); (v) the critical-voltage (CV) electron-beam method. These methods have various strengths and weaknesses, which we briefly review in the light of the requirement that changes in charge density due to bonding should be less than experimental and systematic errors. These changes in low-order X-ray structure factors are normally less than 1%. (Errors quoted in this section are those for X-ray, not electron, structure factors).

The X-ray single-crystal *Pendellösung* method (Aldred & Hart, 1973) is capable of low-order structure-factor measurement with an accuracy of about 0.07% at best. This is about the same or slightly better than the best measurements by the CV and QCBED methods. The disadvantage of this method is that it requires large defect-free single crystals (such as 'dislocation-free' semiconductor wafers), which limits its application, excluding most 'real' crystals, such as $LaMnO_3$. [This is heavily twinned with a twin size of several micrometres (Dechamps *et al.*, 2000).] The data analysis is based on, as in the QCBED method, the perfect crystal theory, which explicitly includes all of the multiple-scattering effects which are otherwise approximated when dealing with extinction in less perfect crystals, as discussed below.

Conventional Bragg X-ray diffraction from inorganic materials normally suffers from large extinction errors affecting the low-order reflections important for studies of bonding (Zuo *et al.*, 2000). This effect has been studied in great detail since the early days, when it was found that differences of one order of magnitude existed between experimental Bragg intensities and the predictions of either the kinematic theory (which predicts angle-integrated intensity proportional to $|F_{\mathbf{g}}|^2$ and to the atomic density squared) or the two-beam dynamical theory (which predicts angle-integrated intensity proportional to $|F_{\mathbf{g}}|$ and to the atomic density, and, without absorption, a reflectivity of unity at the Bragg angle). Primary and secondary extinction may introduce errors of more than 10% if uncorrected, which completely masks any bonding effects. Correction schemes of great sophistication due to Darwin (1922), Zachariasen (1967), Becker & Coppens (1974) and others have been developed [see Becker (1977) for an excellent review and critique]. These methods are based on a mosaic block model, and on attempts to parameterize the effects of crystal shape, multiple scattering and the defects which produce misalignment between blocks. [It has been suggested that dislocations may form low-angle grain boundaries between blocks, and that the scattering from dislocations themselves will dominate bonding effects. These dislocation densities are routinely measured using a transmission electron microscope (TEM); however, a direct correlation between grain boundaries and mosaic blocks has not been established and the mosaic model remains phenomenological.] Humphreys (1999) has pointed out that 'X-ray scattering from the dislocations is typically greater than the scattering from bonding electrons'. Coherent two-beam multiple scattering within each block is included in Darwin's treatment (primary extinction) while incoherent coupling of two-beam intensities describes scattering between blocks (secondary extinction). The more recent general theory, predicting both types, starts with the energy transport equations, but is found to fail if primary extinction is large (Becker, 1977; Becker & Coppens, 1974). That these heroic efforts to develop correction schemes have not been entirely successful can been seen from (i) the fact that differences between structure factors published by different groups greatly exceed their individual experimental (random) errors, suggesting systematic errors, and (ii) the differences between measurements of equivalent reflections. For example, for rutile, after correction for extinction using many careful measurements, Gonschorek (1982) finds $F(1\bar{1}0) = 37.59 + 0.23$ and $F(110) = 38.70 + 0.17$ for the equivalent reflection. Both the erroneous difference between the reflections (owing to extinction) and the standard deviations preclude the observation of bonding modifications. In Cu_2O crystals, the X-ray structure factor $F^x(200) = 78.8$ electrons per unit cell (Zuo *et al.*, 1999), while the measured value by X-ray diffraction is only 90% of this value, owing to extinction effects.

We may conclude that for inorganic crystals a treatment of extinction sufficiently accurate to expose bond modifications to charge density would require a detailed non-statistical description of defects and their scattering. For organic crystals with larger unit cells, where dislocation energies are prohibitively large and where bonding electrons constitute a greater fraction of the total, the situation is much more favourable for conventional X-ray diffraction (Coppens, 1997). Other factors influencing this work include accurate determination of Debye–Waller factors, absorption corrections and polarization corrections. Absorption and extinction corrections depend on crystal shape and quality. The use of very small spherical crystals is therefore indicated.

Bragg γ-ray diffraction at energies up to 400 keV uses radiation whose wavelength is about the same (0.03 Å) as that used for electron diffraction. Primary extinction is reduced when the extinction distance (which increases with beam energy) exceeds the mosaic block size. Secondary extinction y is also reduced, but not eliminated. [In Zachariasen's (1957) two-beam model , extinction $y = (1 + 2aQ)^{-1/2}$, where Q is the scattering strength, proportional to λ^2.] A recent γ-ray diffraction study of Cu_2O crystals (Lippmann & Schneider, 2000) using the Zachariasen model to correct extinction effects initially found significant extinction errors, revealed by correlation between the extinction and multipole parameters. The Bragg profiles and integrated intensities were found to be sensitive to chemical treatment of the crystal surfaces. An attempt was made to obtain extinction-free results by extrapolation to zero wavelength, assuming a Zachariasen model and negligible primary and weak secondary extinction. The effect was to increase the errors in high-order data, and to

introduce scaling problems in combining data sets (Mackenzie & Mathieson, 1992).

The process of extrapolation to zero wavelength assumes the validity of a two-beam model for multiple diffraction. Mackenzie & Mathieson (1992) have pointed out that the structure factors of copper measured by the γ-ray method were 1% lower than the values measured by the dynamical electron diffraction (*Pendellösung*) method. They question the applicability of Darwin's energy-transfer model to these crystals and their imperfections, and suggest the use of other methods (wedge-shaped crystals, profile analysis) for eliminating extinction.

Finally, the CV method of electron diffraction is capable of highly accurate measurements of the ratio of the two structure factors. Errors may be as small as 0.1% [see Spence & Zuo (1992) for a review]. The method is based on three-beam dynamical theory, which may be solved for the wavelength at which, for all thicknesses, destructive interference owing to multiple scattering causes an extinction in the second-order reflection (or higher-order reflections) at the Bragg condition. The resulting condition gives an expression for the ratio of the two structure factors in terms of accelerating voltage. The extinction condition is also a function of excitation error (since three-beam theory contains only products of wavevector and excitation error), hence 'critical-voltage' conditions can be found at many points in CBED patterns where three-beam conditions apply. The disadvantage of this method is that it provides only a ratio. Like all the most accurate methods, errors are limited by knowledge of the Debye–Waller factor.

To test the accuracy of CBED and Bragg X-ray diffraction, refinement results for the 110 reflection in rutile were used as an example. The X-ray diffraction data (Gonschorek, 1982; Restori *et al.*, 1987) were collected at 295 and 100 K in units of electrons per conventional cell. The electron structure factors, measured by CBED, were measured at 115 K, then converted to X-ray structure factors for comparison (Spence & Zuo, 1992), in units of electrons per cell (see Appendix *A* for details). All the values were converted to their corresponding value at 100 K for comparison. Gonschorek's (1982) X-ray refinement result after extinction correction is $F^x(110)$ = 38.896 ($\pm$0.23 or $\pm$0.6%) (at 100 K). Restori *et al.*'s (1987) X-ray refinement result before extinction correction is $F^x(110)$ = 32.8 (at 100 K). Our recent accurate refinement by CBED gives $F^x(110)$ = 37.272 ($\pm$0.009 or $\pm$0.025%) (at 100 K) (Jiang *et al.*, 2001) (the error analysis is obtained by averaging several measurements).

Zuo *et al.* (2000) have used the Zachariasen (1967) two-beam model to correct extinction effects in X-ray diffraction data for Cu_2O crystals. For the strong low-order 111 and 200 reflections of Cu_2O crystals, the associated error in the structure factors before extinction correction is about 10%; after extinction correction, it is about 1%, which is insufficient to see the changes in charge density due to bonding.

The accuracy of the QCBED method results from two factors. Firstly, the nanoscale electron probe size is smaller than one mosaic block, and hence the perfect-crystal Bloch-wave many-beam theory can be applied with confidence. Extinction effects [and absorption (Zuo, 1998)] are thus either fully accounted for or absent, depending on one's point of view. The region from which data is collected can be imaged at near-atomic resolution in the TEM to ensure that defects are not present. Secondly, the Mott–Bethe formula (Spence & Zuo, 1992) relating electron structure factors to X-ray structure factors shows a large enhancement of electron scattering factors at small angles, owing to the effect of Poisson's equation, which relates the charge density, which diffracts X-rays, to the potential, which diffracts electrons.

Finally, we summarize the major differences (advantages and disadvantages) between Bragg X-ray diffraction and QCBED. The advantage of Bragg X-ray diffraction is its ability to measure high-order reflections very accurately; thus, it can be used to determine atom coordinates, temperature factors *etc.* The main disadvantage is the large measurement error for strong low-order reflections owing to extinction. The advantage of QCBED is its ability to measure the absolute values of a few low-order structure factors accurately. The disadvantage is that the crystal structure and thermal parameters must be known. It is clear that Bragg X-ray and QCBED methods complement each other. The advantages of each may now be combined to allow charge-density mapping in favourable cases with an accuracy increased by an order of magnitude.

3. Orbital ordering model

For an isolated 3*d* ion, the five *d*-orbital states are degenerate. In a crystal with octahedral coordination, the five *d* orbitals are split by the crystal field into three t_{2g} [$d(xy)$, $d(yz)$, $d(zx)$] orbitals and two e_g [$d(3x^2 - r^2)$, $d(x^2 - y^2)$] orbitals. In $LaMnO_3$ crystals, the elongation of MnO_6 octahedra, owing to the cooperative JT distortion, further splits the t_{2g} and e_g orbitals. Fig. 1 shows the schematic splitting of the *d*-electron orbitals in Mn^{3+} in an $LaMnO_3$ crystal. For the two e_g orbitals, $3d(3z^2 - r^2)$ orbitals have lower energy than $3d(x^2 - y^2)$ orbitals. According to Hunda's law and to the Fermi–Dirac statistical distribution theory, the four 3*d* electrons in an Mn^{3+} ion will first occupy the four lower-energy orbitals with the same spin direction, which are three t_{2g} orbitals and one lower-

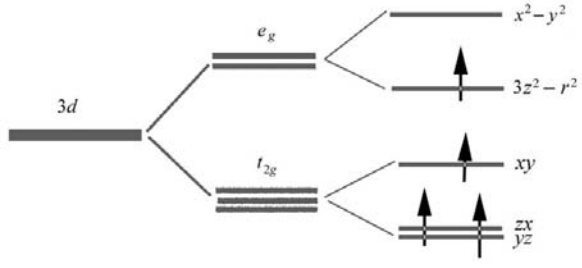

Figure 1
Schematic graph of 3*d* orbital splitting. A cubic crystal field will split the 3*d* orbital into e_g and t_{2g} orbitals. JT distortion in $LaMnO_3$ will further split Mn^{3+} $3d$(e_g and t_{2g}) orbitals. Four 3*d* electrons of Mn^{3+} will occupy the four lower-energy orbitals.

energy e_g orbital, which is the $3d(3z^2 - r^2)$ orbital. This is the driving force for the $3d(3z^2 - r^2)$ orbital ordering.

We have adopted the model of $3d(3z^2 - r^2)$ orbital ordering of Mn^{3+} in $LaMnO_3$ given elsewhere (Hotta *et al.*, 1999; Bala & Oles, 2000; Murakami *et al.*, 1998; Rodriguez-Carvajal *et al.*, 1998). Fig. 2 shows a schematic diagram of $3d(3z^2 - r^2)$ electron ordering of Mn^{3+} in an $LaMnO_3$ crystal projected along the *c* axis. The actual orbital direction is slightly tilted from the *ab* plane owing to the oxygen octahedral tilting. The $3d(3z^2 - r^2)$ orbital is always directed towards the most remote O atoms. The local origin was selected at one Mn^{3+} ion, with the *z* axis directed from the Mn^{3+} site to one of the remote O atoms, and the *x* and *y* axes to the nearest O atoms in the *c* and *a* directions. The other three Mn^{3+} ions' coordinate systems were then obtained by symmetry operations.

4. Structure-factor calculations

4.1. Atomic scattering factors for non-spherical orbitals

The scattering factor depends upon atomic orientation if the atomic charge density is non-spherical. An example is the 222 reflection in silicon, which is kinematically forbidden within the spherical-atom approximation, but is finite with non-spherical bonding.

Atomic scattering factors for non-spherical atoms have been studied by McWeeny (1951), Freeman (1959), Dawson (1964*a*,*b*) and Weiss & Freeman (1959). For aspherical atoms, the direction of the scattering vector with respect to the symmetry axis of an atom must be considered in order to calculate the atomic scattering factor. Calculations for *d* orbitals have been performed by Freeman (1959) and Weiss & Freeman (1959).

For the atomic scattering-factor calculation, the basic scattering matrix elements can be written as

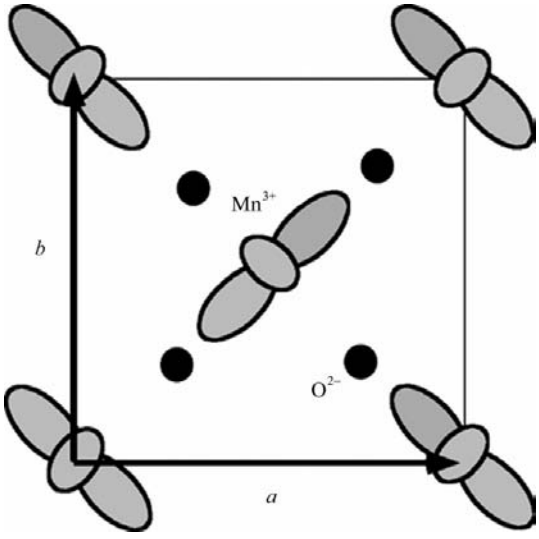

Figure 2
Schematic view of the orbital ordering in the *ab* plane of $LaMnO_3$. The orbital ordering along the *c* axis is expected to repeat the same pattern.

$$f_{ij}(\mathbf{s}) = \int \rho_{ij}(\mathbf{r}) \exp(i\,\mathbf{S}\cdot\mathbf{r})\,\mathrm{d}v = \int \varphi_i^* \varphi_j \exp(i\,\mathbf{S}\cdot\mathbf{r})\,\mathrm{d}\mathbf{r}, \quad (1)$$

where $\mathbf{S}$ is the scattering vector, with the modulus $|\mathbf{S}| = 4\pi\sin(\theta)/\lambda$, λ is the wavelength of the incident radiation, $\rho_{ij} = \varphi_i\varphi_j$ is the atom charge density and φ_i is an individual one-electron wave function. For a non-spherical atomic charge density, the observed scattering depends upon the scattering vector $\mathbf{S}$.

Expand $\exp(i\mathbf{S}\cdot\mathbf{r})$ into

$$\exp(i\,\mathbf{S}\cdot\mathbf{r}) = 4\pi \sum_{l=0}^{\infty} \sum_{m=-l}^{l} i^l j_l(Sr) Y_{lm}(\beta,\gamma) Y_{lm}^*(\theta,\phi), \quad (2)$$

where j_l is an lth-order spherical Bessel function, β and γ are angular coordinates of $\mathbf{S}$, and θ and ϕ are angular coordinates of $\mathbf{r}$.

Substitute (2) into (1) and write the single-electron wave function as $\varphi_i = R_i(r)\Theta_l^m(\theta)\Phi_m(\phi)$, substitute into (1) and separate the spherical harmonic function into products of normalized associate Legendre functions. The result is

$$\begin{aligned} f_{ij} &= (4\pi)^{1/2} \sum_n i^n (2n+1)^{1/2} C^n\big(l_i m_i, l_i m_j\big) \Theta_n^{m_i - m_j} \\ &\quad \times (\cos\beta)\Phi_{m_i - m_j}(\gamma) \int_0^{\infty} R_i R_j j_n(Sr)\,\mathrm{d}r \\ &= (4\pi)^{1/2} \sum_n i^n (2n+1)^{1/2} C^n\big(l_i m_i, l_i m_j\big) \Theta_n^{m_i - m_j} \\ &\quad \times (\cos\beta)\Phi_{m_i - m_j}(\gamma) \langle j_n \rangle_{ij}, \end{aligned} \quad (3)$$

where $C^n(l_i m_i, l_i m_j)$ are the integrals of the product of three associated Legendre functions. These have been tabulated by Condon & Shortley (Weiss & Freeman, 1959). $S = 4\pi\sin(\theta)/\lambda$ and $j_n(Sr)$ are spherical Bessel functions.

Equation (3) clearly indicates that the scattering-matrix elements can be written as linear combinations of $\langle j_n \rangle_{ij}$, which have been tabulated in *International Tables for X-ray Crystallography* (Ibers & Hamilton, 1974) using Hartree–Foch (HF) wave functions.

If we assume $m_i = m_j$, then (3) reduces to

$$f_{ij} = \sum_n i^n (2n+1) C^n(l_i m_i, l_i m_i) P_n(\cos\beta) \langle j_n \rangle_{ij}. \quad (4)$$

$P_n(\cos\beta)$ is the ordinary Legendre function.

Using (3) and (4), Freeman (1959) and Weiss & Freeman (1959) have deduced formulae in a more concise expression for different orbitals.

For *d* electrons, when $i = j$, $\beta = 0$, the principal scattering factors, f_{ii} (written as f_i for short), are obtained from (4),

$$\begin{aligned} f_2(d) &= \langle j_0 \rangle + \tfrac{10}{7}\langle j_2 \rangle + \tfrac{3}{7}\langle j_4 \rangle, \\ f_1(d) &= \langle j_0 \rangle - \tfrac{5}{7}\langle j_2 \rangle - \tfrac{12}{7}\langle j_4 \rangle, \\ f_0(d) &= \langle j_0 \rangle - \tfrac{10}{7}\langle j_2 \rangle + \tfrac{18}{7}\langle j_4 \rangle. \end{aligned} \quad (5)$$

When $\beta \neq 0$, the principal scattering factors are expressed in prime format, and can be written as a linear combination of the principal scattering factors $f_2(d)$, $f_1(d)$ and $f_0(d)$,

$$
\begin{aligned}
f_2(d) &= \tfrac{1}{8}\left[1 + 6\cos^2(\beta) + \cos^4(\beta)\right] f_2(d) + \tfrac{1}{2}\left[1 - \cos^4(\beta)\right] f_1(d) \\
&\quad + \tfrac{3}{8}\left[1 - 2\cos^2(\beta) + \cos^4(\beta)\right] f_0(d), \\
f_1(d) &= \tfrac{1}{2}\left[1 - \cos^4(\beta)\right] f_2(d) + \left[\tfrac{1}{2} - \tfrac{3}{2}\cos^2(\beta) + 2\cos^4(\beta)\right] f_1(d) \\
&\quad + \tfrac{3}{2}\left[\cos^2(\beta) - \cos^4(\beta)\right] f_0(d), \\
f_0(d) &= \tfrac{3}{4}\left[1 - 2\cos^2(\beta) + \cos^4(\beta)\right] f_2(d) \\
&\quad + 3\left[\cos^2(\beta) - \cos^4(\beta)\right] f_1(d) \\
&\quad + \left[\tfrac{1}{4} - \tfrac{3}{2}\cos^2(\beta) + \tfrac{9}{4}\cos^4(\beta)\right] f_0(d). \qquad (6)
\end{aligned}
$$

For t_{2g} orbitals, the scattering factor is

$$
f'(t_{2g}) = \tfrac{1}{3}\left[2f'_1 + f'_2 - \tfrac{1}{2}(f'_{2,-2} + f'_{-2,2})\right]. \qquad (7)
$$

The individual e_g orbitals are expressed as follows:

$$
\begin{aligned}
f'(x^2 - y^2) &= f'_2 + \tfrac{1}{2}(f'_{2,-2} + f'_{-2,2}) \\
f'(3z^2 - r^2) &= f'_0,
\end{aligned} \qquad (8)
$$

where $f_{2,-2}$ is a cross term, from (3),

$$
\begin{aligned}
f'_{2,-2} &= \tfrac{15}{8}\sin^4(\beta)\exp(i\,4\gamma)\langle j_4\rangle, \\
f'_{2,-2} &= f'^{*}_{-2,2}.
\end{aligned} \qquad (9)
$$

Equations (5)–(9) will be used in the calculations.

4.2. The non-spherical Mn^{3+} ionic scattering factor in $LaMnO_3$

In order to calculate the scattering factor of non-spherical Mn^{3+} ions, the angular coordinates β and γ of the scattering vector **S** in the local Mn^{3+} atomic coordinate system must be determined. A coordinate-system transformation matrix is required to transform the scattering vector from the crystal to the atomic coordinate system so that the angular coordinates β and γ could be calculated. According to the orbital ordering model given in §2, the Mn^{3+} ion at $(\frac{1}{2}, 0, 0)$ is selected for finding the transformation matrix between the crystal and atomic coordinate system. Using atomic coordinates given elsewhere (Rodriguez-Carvajal *et al.*, 1998), we found the transformation matrix (TM) for this Mn^{3+} ion as

$$
\mathrm{TM} = \begin{bmatrix} 0.2038 & 0.0207 & -0.9788 \\ -0.7972 & 0.5839 & -0.1536 \\ 0.5683 & 0.8116 & 0.1355 \end{bmatrix}. \qquad (10)
$$

A given scattering vector $\mathbf{S}_{\mathrm{crystal}} = (x_c, y_c, z_c)$ can be transformed into the local Mn^{3+} atomic coordinate system $\mathbf{S}_{\mathrm{atomic}} = (x_a, y_a, z_a)$. It is

$$
\mathbf{S} \equiv \begin{pmatrix} x_a \\ y_a \\ z_a \end{pmatrix} = \mathrm{TM} \times \mathbf{S}_{\mathrm{cryst}} \equiv \mathrm{TM} \times \begin{pmatrix} x_c \\ y_c \\ z_c \end{pmatrix}. \qquad (11)
$$

Therefore, angular coordinates β and γ can be obtained,

$$
\beta = \cos^{-1}(z_a/|\mathbf{S}_a|), \qquad \gamma = \tan^{-1}(y_a/x_a). \qquad (12)
$$

By substituting (12) into (6) and (9), the non-spherical Mn^{3+} ionic scattering factor in an $LaMnO_3$ crystal can be obtained.

The other three Mn^{3+} ions' local atomic coordinate systems are obtained by applying symmetry operations, which are the products of the symmetry operation matrix and the TM matrix. The same method can be used to calculate their scattering factors.

4.3. Structure-factor calculations for $LaMnO_3$

To calculate the structure factors of an $LaMnO_3$ crystal, cell constants, atom coordinates and thermal parameters were taken from Rodriguez-Carvajal *et al.* (1998). To show the effect of orbital ordering, the electronic configuration used for Mn^{3+} ions was $3d^4(t_{2g}^3 e_g^1)$, the e_g electron is assumed to be a hybridized wave function $\psi = x\,\varphi[3d(3z^2 - r^2)] + (1 - x)\,\varphi[3d(x^2 - y^2)]$, of which x is the electron population on the $3d(3z^2 - r^2)$ orbital. Ionic scattering factors were used for La^{3+} and O^{2+}, calculated by the Dirac–Fock method. The charge density of the O^{2-} ion was calculated using a Watson sphere of radius 1.2 Å; this is the value that gives the best fit to experiment in the case of MgO (Zuo *et al.*, 1999). For the Mn^{3+} ion, the tabulated value in *International Tables for X-ray Crystallography* (Ibers & Hamilton, 1974) was used, calculated using HF wave functions and taking the orbital ordering of $3d(3z^2 - r^2)$ into consideration. Both X-ray structure factors (with F_g in units of electrons per cell) and electron structure factors (V_g, which is a Fourier coefficient of crystal potential in units of volts) were calculated. The Mott formula (Spence & Zuo, 1992) was used to obtain electron structure factors from X-ray atomic scattering factors.

5. Results and discussions

5.1. Electron structure factors of $LaMnO_3$

Calculations were completed for the low-order structure factors of $LaMnO_3$ with different electron occupancy x on the $3d(3z^2 - r^2)$ orbital of the Mn^{3+} ion. Both X-ray and electron structure factors *versus* the occupancy of the $3d(3z^2 - r^2)$ orbital are listed in Table 1. The electron population x is the electron occupancy on the $3d(3z^2 - r^2)$ orbital. $x = 0.5$ corresponds to one e_g electron equally occupying two e_g orbitals, in which case there can be no orbital ordering since all orbitals are equivalent; on the other hand, $x = 1$ represents the e_g electron occupying the $3d(3z^2 - r^2)$ orbital only, which corresponds to complete orbital order. Only the low orders with larger structure-factor changes are listed in the table. The results clearly indicate the strong effect of orbital ordering on electron structure factors, up to 11% for weak reflections and 1.45% for strong reflections. For X-ray structure factors, the orbital order effect is very small, around 0.1–0.3% for the stronger reflections.

Fig. 3 shows the electron structure factors of the 110 reflection $[V_g(110)]$ *versus* electron population on $3d(3z^2 - r^2)$ (orbital order). It increases linearly with the occupancy of the $3d(3z^2 - r^2)$ orbital. This property could possibly be used in experiments for measuring the electron occupancy on the $3d(3z^2 - r^2)$ orbital.

5.2. Charge-density map of $LaMnO_3$

A charge-density difference map was obtained using an occupancy of the electron orbital between $x = 0.5$ and $x = 1$,

Table 1
Electron and X-ray structure factors of six low-order reflections of an $LaMnO_3$ crystal.

$V_g(hkl)$ are the Fourier transformation coefficients of the crystal potential in units of volts. $F^x(hkl)$ are the Fourier transformation coefficients of the crystal charge density in units of electrons. The $3de_g$ electron population configuration is $x\Psi[3d(3z^2 - r^2] + (1 - x)\Psi[3d(x^2 - y^2)]$.

		Electron population x on $3d(3z^2 - r^2)$ orbital of an Mn^{3+} ion			
	Diffraction spot	$x = 0.5$	$x = 0.8$	$x = 1$	Structure change ratio
Electron structure factors	$V(101)$	0.451	0.444	0.440	−2.5%
	$V(110)$	2.593	2.580	2.572	−0.85%
	$V(002)$	2.860	2.885	2.904	−1.45%
	$V(020)$	8.006	8.031	8.048	0.52%
	$V(120)$	0.945	0.972	0.990	4.5%
	$V(210)$	0.416	0.391	0.374	11%
X-ray structure factors	$F(101)$	10.614	10.631	10.643	0.26%
	$F(110)$	82.613	82.657	82.686	0.089%
	$F(002)$	92.171	92.080	92.019	0.16%
	$F(020)$	215.07	214.91	214.80	0.13%
	$F(120)$	24.249	24.030	23.884	−1.5%
	$F(210)$	9.555	9.769	9.912	−3.6%

which corresponds to the $3d(3z^2 - r^2)$ orbital half and completely filled. The charge difference map was obtained by the Fourier synthesis method, using 15996 Fourier coefficients, equal to a sphere of 2.5 $Å^{-1}$ in reciprocal space. The three-dimensional rendering of the charge difference is striking (Fig. 4*a*). It clearly shows the shape of the $3d(3z^2 - r^2)$ and $3d(x^2 - y^2)$ orbitals. The blue region shows a total of 0.5 electron deficiency with a $3d(x^2 - y^2)$ hole. The green region has a 0.5 electron gain in the $3d(3z^2 - r^2)$ orbital. The charge-density difference map along the *c* axis in Fig. 4(*b*) gives similar results to the schematic figures of Murakami *et al.* (1998). This charge-density difference could be mapped by combining X-ray diffraction to measure the high-order reflections with QCBED to measure the low orders, and so to give direct evidence for the $3d(3z^2 - r^2)$ orbital ordering.

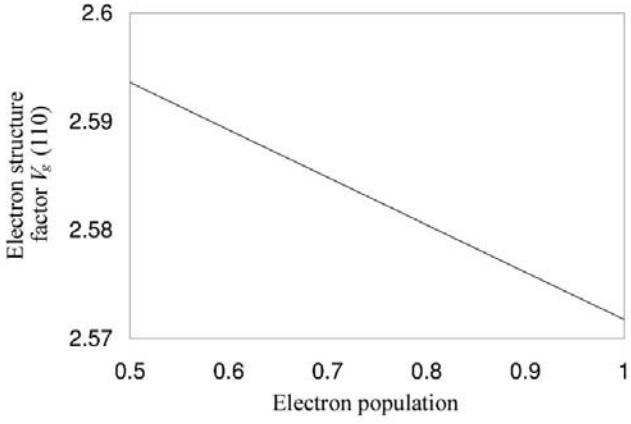

Figure 3
Electron structure factors of the 110 reflection of an $LaMnO_3$ crystal $Vg(110)$ *versus* electron population on the $3d(3z^2 - r^2)$ orbital, $x = 0.5$ and $x = 1$ corresponding to totally non-ordered and ordered, respectively. The linearity of the relationship may be used to determine the electron populations in the Mn^{3+} $3d(3z^2 - r^2)$ orbital.

5.3. Discussion

From these calculations, we clearly see the effect of the orbital ordering on structure factors, particularly on electron structure factors. This suggests to us an opportunity that orbital ordering in $LaMnO_3$ crystals can be observed directly by structure-factor measurement to map the charge density.

The question arises as to where the CV method can measure changes in the ratio of the **g** and 2**g** (or other higher-order reflections) structure factors and hence observe the orbital ordering. In a real crystal, the changes in the ratio measured by CV come not only from the orbital ordering effect (*i.e.* changes in atomic orbitals) but also from bonding (*i.e.* charge transfer), and the accuracy is limited by knowledge of the Debye–Waller factor. Hence, changes in the ratio cannot be used as an indication of orbital ordering. Only a charge-density map can provide evidence of orbital ordering.

The X-ray structure factor changes by 0.26% or less for the stronger reflections. For Bragg X-ray diffraction, the best accuracy which can be reached is about 0.5% after extinction correction (Fox, 1993). For higher-order stronger reflections, the X-ray structure-factor changes are around 0.3% or less owing to orbital ordering, beyond the X-ray accuracy limit. Thus, Bragg X-ray diffraction alone cannot detect orbital order in $LaMnO_3$ crystals.

The changes in electron structure factors are large, up to 1.45% for the stronger reflections, enough for QCBED. Our recent refinement results on cuprite, silicon and rutile give an accuracy for V_g of about 0.3% (Zuo *et al.*, 1999; Ren *et al.*, 1997; Jiang *et al.*, 2001). The three strong reflections of $LaMnO_3$, $V(110)$, $V(002)$ and $V(020)$, change by −0.85, −1.45 and 0.52%, respectively, owing to orbital ordering, which are within our refinement limits. This suggests that this method can be used to obtain $3d(3z^2 - r^2)$ orbital-ordering information and to provide direct evidence of orbital order. However, accurate X-ray measurements for the high-order reflections are required to obtain a complete charge-density map and to determine the temperature factors.

We emphasize here that the electron structure factor is more sensitive to the bonding electrons which mainly contribute to low-order reflections. For scattering vectors greater than about 1.0 Å^{-1}, X-ray diffraction rapidly becomes much more accurate. For the orbital ordering in $LaMnO_3$ crystals, only electron diffraction by QCBED can be expected to detect the orbital ordering directly.

6. Conclusions

A brief comparison has been made of various methods of accurate structure-factor measurement. X-ray and electron structure factors of $LaMnO_3$ have been calculated using a non-spherical Mn^{3+} model as a function of orbital occupancy. The electron structure factors are significantly altered due to orbital ordering of the $3d(3z^2 - r^2)$ orbital of the Mn^{3+} ion, and this change should be measurable by quantitative CBED. By contrast, the calculated X-ray structure factors show a very small change, which probably cannot be measured by conventional Bragg X-ray diffraction. New measurements of a structure factor in rutile by QCBED are reported, and these are compared with Bragg X-ray values. The results confirm that QCBED can provide accurate extinction-free measurements of low-order structure factors, which is extremely difficult or perhaps impossible to obtain when using other methods applied to real inorganic crystals.

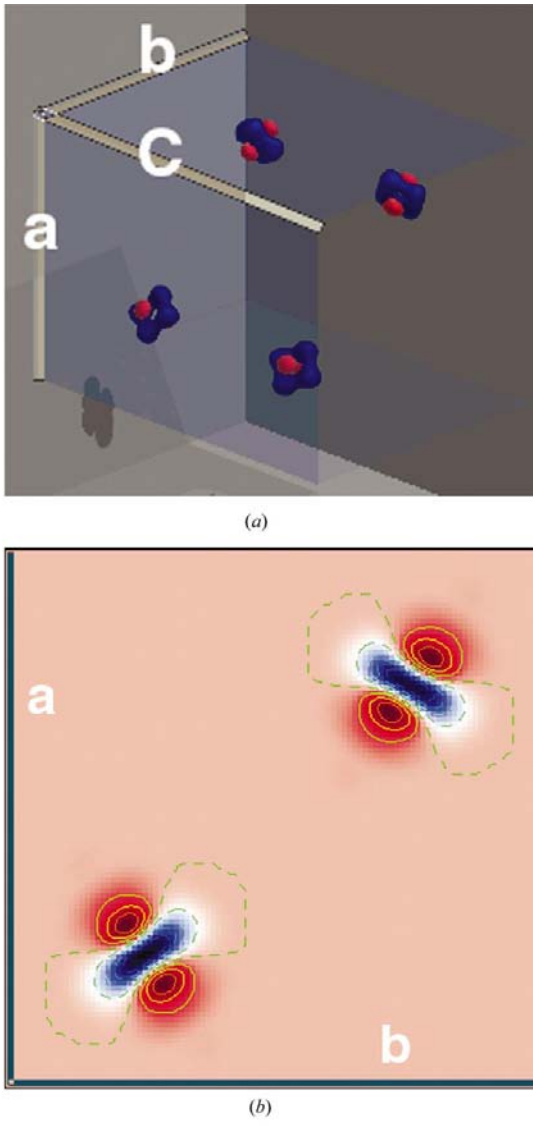

Figure 4
Charge-density difference map of an $LaMnO_3$ crystal between the $3d(3z^2 - r^2)$ orbital ordered ($x = 1$) and non-ordered ($x = 0.5$) state. (Note that Mn^{3+} ions are shifted inside the cell for display.) (*a*) Three-dimensional rendering of the charge difference map. The blue region shows a $3d(x^2 - y^2)$ orbital hole (no electron). The red region shows a $3d(3z^2 - r^2)$ orbital with one electron in it. (*b*) Two-dimensional charge-density difference map. The contour line increment is 0.2 e Å^{-2}. The dashed line represents the electron gain area. The solid line represents the electron loss area.

APPENDIX *A*
Calculation of X-ray structure factor $F^x(110)$ from measured electron structure factor $U(110)$

The relationship between the X-ray structure factor and electron structure factor can be written as (Spence & Zuo, 1992)

$$F^x_{\mathbf{g}} = \sum_{ij} Z_i \exp\left(-\beta_{ji} h_i h_j\right) \exp(-2\pi i\, \mathbf{g}\cdot\mathbf{r}_i) - (C\Omega s^2/\gamma) U_{\mathbf{g}}, \tag{13}$$

where Z_i is the atomic number, β_{ij} are the anisotropic temperature factors, h_i ($i = 1, \ldots, 3$) are the Miller indices of a reflection $\mathbf{g}$, $\mathbf{r}_i$ is the atomic position vector, C is a constant, $s = 2\pi \sin(\theta_B)/\lambda$, where θ_B is the Bragg angle and λ is the wavelength of radiation, Ω is the cell volume, γ is a relativistic constant and $U_{\mathbf{g}}$ is the measured electron structure factor. C = 131.2625 if s, Ω and $U_{\mathbf{g}}$ are given in Å.

In order to convert the X-ray from one temperature to another temperature, the following approximation formula is used:

$$\frac{F^x_{\mathbf{g}}(T_2)}{F^x_{\mathbf{g}}(T_1)} = \frac{\sum_{ij} f_i(s_2) \exp[-\beta_{ij}(T_2) h_i h_j] \exp[-2\pi i\, \mathbf{g}\cdot\mathbf{r}_i(2)]}{\sum_{ij} f_i(s_1) \exp[-\beta_{ij}(T_1) h_i h_j] \exp[-2\pi i\, \mathbf{g}\cdot\mathbf{r}_i(1)]}, \tag{14}$$

where T_1 and T_2 represent temperatures and $f_i(s)$ are the scattering factors of the atoms. In a crystal, because of the bonding effects, $f_i(s)$ is unknown. A neutral atomic model was used for approximate conversion.

The measured electron structure factor $U_{\mathbf{g}}(110)$ for rutile is 0.06370 (±0.00018) Å^{-2} (at 115 K, acceleration voltage is 119.52 V). All the temperature factors and crystal constants were taken from the most accurate measurements reported by Burdett *et al.* (1987). Using (14), the calculated X-ray structure factor is $F^x(110)$ = 37.247 (±0.009) electrons per unit cell at 115 K. Using (14), the X-ray structure factor at 100 K is 37.272 (±0.009) electrons per unit cell.

We thank Mike Steven for discussions. This work was funded by NSF award DMR 9973894.

References

Aldred, P. J. & Hart, M. (1973). *Proc. R. Soc. London Ser. A*, **332**, 223–238.
Bala, J. & Oles, A. M. (2000). *Phys. Rev. B*, **62**(10), R6085–R6088.
Becker, P. J. (1977). *Acta Cryst.* A**33**, 243–249.
Becker, P. J. & Coppens, P. (1974). *Acta Cryst.* A**30**, 129–147.
Burdett, J. K., Hughbanks, T., Miller, G. J., Richardson, J. W. & Smith, J. V. (1987). *J. Am. Chem. Soc.* **109**(12), 3639–3646.
Coppens, P. (1997). X-*ray Charge Densities and Chemical Bonding*. Oxford University Press.
Darwin, C. G. (1922). *Philos. Mag.* **43**, 800.
Dawson, B. (1964*a*). *Acta Cryst.* **17**, 990–996.
Dawson, B. (1964*b*). *Acta Cryst.* **17**, 997–1009.
Dechamps, M., Guevara, A. M., Pinsard, L. & Revcolevschi, A. (2000). *Philos. Mag. A*, **80**(1), 119–127.
Fox, A. G. (1993). *Philos. Mag. Lett.* **68**(1), 29–37.
Freeman, A. J. (1959). *Acta Cryst.* **12**, 261–270.
Gonschorek, W. (1982). *Z. Kristallogr.* **169**, 187–203.
Goodenough, J. B. (1997). *J. Appl. Phys.* **81**(8), 5330–5335.
Hotta, T., Yunoki, S., Mayr, M. & Dagotto, D. (1999). *Phys. Rev. B*, **60**(22), R15009–R15012.
Humphreys, C. J. (1999). *Nature (London)*, **401**, 21–22.
Ibers, J. A. & Hamilton, W. C. (1974). Editors. *International Tables for X-ray Crystallography*, Vol. IV. Birmingham: Kynoch Press.
Jiang, B., Zuo, J. M., Friis, J. & Spence, J. C. H. (2001). Submitted.
Lippmann, T. & Schneider, J. R. (2000). *J. Appl. Cryst.* **33**, 156–167.
Mackenzie, J. K. & Mathieson, A. M. (1992). *Acta Cryst.* A**48**, 231–236.
McWeeny, R. (1951). *Acta Cryst.* **4**, 513–519.
Murakami, Y., Hill, J. P., Gibbs, D., Blume, M., Koyama, I., Tanaka, M., Kawata, H., Arima, T. & Tokura, Y. (1998). *Phys. Rev. Lett.* **81**(3), 582–585.
Radaelli, P. G., Cox, D. E. & Marezio, M. (1997). *Phys. Rev. B*, **55**(5), 3015–3023.
Ren, G., Zuo, J. M. & Peng, L. M. (1997). *Micron*, **28**, 459–467.
Restori, R., Schwarzenbach, D. & Schneider, J. R. (1987). *Acta Cryst.* B**43**, 251–257.
Rodriguez-Carvajal, J., Hennion, M., Moussa, F. & Moudden, A. H. (1998). *Phys. Rev. B*, **557**(6), R3189–R3192.
Spence, J. C. H. & Zuo, J. M. (1992). *Electron Microdiffraction.* New York: Plenum Press.
Weiss, R. J. & Freeman, A. J. (1959). *J. Phys. Chem. Solids*, **10**, 147–161.
Wollan, E. O. & Koehler, W. C. (1955). *Phys. Rev.* **100**, 545–563.
Zachariasen, W. H. (1967). *Acta Cryst.* **23**, 558–564.
Zuo, J. M. (1998). *Mater. Trans. JIM*, **39**(9), 938–946.
Zuo, J. M., Kim, M., O'Keeffe, M. & Spence, J. C. H. (1999). *Nature (London)*, **401**, 49–52.
Zuo, J. M., O'Keefffe, M., Kim, M. & Spence, J. C. H. (2000). *Angew. Chem. Int. Ed. Engl.* **39**(21), 3791–3794.